

X-661-74-335

PREPRINT

NASA TM X-70802

COSMIC RAY COMPOSITION MEASUREMENTS AND HIGH ENERGY IONIZATION SPECTROMETERS

(NASA-TM-X-70802) COSMIC RAY COMPOSITION
MEASUREMENTS AND HIGH ENERGY IONIZATION
SPECTROMETERS (NASA) 44 p HC \$3.75 CSCL 03B

N75-15582

Unclas

G3/93 07329

JOHN F. ARENS
JONATHAN F. ORMES

NOVEMBER 1974



GSFC

— GODDARD SPACE FLIGHT CENTER —

GREENBELT, MARYLAND



"This paper presents the views of the author(s), and does not necessarily reflect the views of the Goddard Space Flight Center, or NASA."

**For information concerning availability
of this document contact:**

**Technical Information Division, Code 250
Goddard Space Flight Center
Greenbelt, Maryland 20771**

(Telephone 301-982-4488)

COSMIC RAY COMPOSITION MEASUREMENTS
AND HIGH ENERGY IONIZATION SPECTROMETERS

John F. Arens

and

Jonathan F. Ormes

NASA/Goddard Space Flight Center
Greenbelt, Maryland 20771

ABSTRACT

Element abundances of cosmic rays Li through Si with energy above 0.8 GeV/amu were measured on a balloon borne instrument containing a total absorption ionization spectrometer. Statistical techniques were used to analyze the five measurements of each particle to determine its charge and energy. The technique allows a determination of systematic errors to be made. Corrections for Landau fluctuations, spark chamber inefficiency, and background particles were included. Comparison with other published results is made. Differences in the shape of the spectrum determined from measurements of different workers indicate that the absolute intensity is still known to only $\pm 15\%$ between 2 and 10 GV/c rigidity.

INTRODUCTION

In order to study the composition and energy spectra of multiply charged cosmic ray nuclei we have flown an ionization spectrometer on balloons^{1,2}. In the principal balloon flight with this instrument we found a dramatic difference in the differential spectra of iron and carbon and oxygen nuclei³. A similar difference has been observed by Juliusson⁴. Because of the profound implications of these measurements^{5,6} for the nature of the cosmic ray sources and because of some quantitative differences of these measurements with those of other workers^{4,7}, we have undertaken a study of the systematic effects which might have influenced our earlier results. As we² and Webber⁷ in his review article noted previously, our fluxes of carbon and oxygen were somewhat lower than those reported by other workers. We speculated that this might be due to back-scattering from the massive spectrometer used to measure the energy.

These effects were checked using instruments on a balloon flight whose primary objective was a measurement of the cosmic ray electrons⁸. A schematic cross section of the instrument is shown in Figure 1. The spectrometer was sufficiently deep to measure electron energies (18 radiation lengths), but was not deep enough to measure nucleon energies with good accuracy. It was sufficiently deep for nuclear interactions to take place, and so will produce backscattering effects if they are important. The charge detection section of the experiment included two Cerenkov detectors and two plastic scintillators. This four fold charge detection scheme was an improved version of that used previously.

The particle trajectories were measured using a wire grid spark chamber. On this flight an 8 deck chamber was used in contrast to the 4 deck chamber previously flown. A new more accurate trajectory determining algorithm was used⁹ which is able to eliminate spurious sparks from delta rays of the heavy nuclei¹⁰. This algorithm also can find multiple trajectories to look at the effects of interacting particles, atmospheric showers, etc.

We shall show in this paper that this more sophisticated detector allows us to conclude that the largest uncertainty in our previous results was due to uncertainties in the efficiency of the spark chamber, and not due to backscattering. We present here our results on the flux and charge composition between Li and Si at a geomagnetic cutoff of 2.9 Gv/c. The results are compared with those of other workers^{11,12} from this same latitude. Systematic differences are discussed. There are discrepancies not only in intensity but also in the spectral shape between 2 and 10 Gv/c.

EXPERIMENT

The apparatus has been described by Silverberg⁹ and was launched on a balloon from Cape Girardeau, Missouri on October 1, 1972. It drifted less than 200 miles from the launch site before landing. The geomagnetic cutoff is 2.9 Gv/c.

The elements in the charge detection section of this experiment were similar to those previously flown except that a previously used CsI mosaic scintillator was replaced by a Cerenkov detector. The two plastic scintillators were 50cm x 50cm Pilot B and measured the ionization

loss rate of the particles (S_1 under 1.94 gm/cm^2 of matter). Two Cerenkov detectors were the other charge measuring elements. One was a piece of Pilot 425 (acrylic plastic with a wave shifter) viewed edge on through adiabatic light pipes by four photomultiplier tubes. The other was a piece of fused silica in a white box viewed by four PMT's. Because the flight was designed to look at electrons, the phototubes for both these Cerenkov detectors were linear only to $Z \geq 16$, and so no results above this charge were obtained.

It was not possible to completely reconcile the response of the two Cerenkov detectors as a function of β . The edges of the fused silica crystal were blocked by support brackets, and even though the surface was roughened by sand blasting there apparently was still considerable total internal reflection at large angles of incidence. In the crystal with wave shifter, apparently less than $\frac{1}{3}$ of the collected light is shifted and isotropized. The effects of light collection are complicated as the cone angle of the light varies with velocity and the internal reflection of this light depends on the incident angle of the particle. The net result is that the two detectors had different responses as a function of velocity and zenith angle. The differences were at the $\pm 10\%$ level and have been ignored in this analysis. However, they made it impossible to unravel energy spectra from the Cerenkov response. Similar effects could be important in experiments in which a single C detector is used to determine velocity^{11,12}.

The tungsten modules shown in Figure 1 are made of 1 radiation length slabs of tungsten and plastic scintillators and they constitute

the energy spectrometer. It was designed for studying electron cascade showers, but at low energy (for $\beta \leq 0.9$) its response was proportional to energy for heavy nuclei. In this energy range the energy deposit is dominated by ionization loss. This was verified by scatter plots of the Cerenkov and the spectrometer responses. At high energies ($\beta > 0.9$) the spectrometer is so thin that the response depends strongly on the location of the first interaction. This effect could be drastically reduced by placing constraints on the location of the first interaction; because of the consequent reduction in statistical significance of the data this analysis has not been done.

DATA ANALYSIS

The data for each event consisted of a spark chamber readout and five pulse height measurements. The pulse heights, of two scintillators, two Cerenkov counters, and the summed spectrometer, were corrected by empirical calibration curves to put them in units of minimum ionizing muons. Using the trajectory as determined by the spark chamber, the two scintillator and two Cerenkov signals were normalized to vertical incidence. Non uniformities as a function of position in these four detectors were removed by simple maps. Each detector was divided into $5 \times 5 = 25$ squares and the average pulse height of oxygen in each square was found. A simple function over area that described these average pulse heights at the center of each square was created for each detector and was used as the mapping correction divisor. The detectors were adequately uniform for this technique to work; the uncorrected oxygen pulse heights were far enough removed from the nitrogen and neon

pulse heights and fluorine is sufficiently rare that a "beam" of oxygen could be used. The four charge detectors were then normalized to the same pulse height for relativistic oxygen nuclei.

Spark chamber trajectories of all events were required to exit the bottom of the spectrometer. The energy deposited in the spectrometer was found by summing the pulse heights in the several layers of scintillator and multiplying by 8.17 MeV/ μ on as determined in a calibration run at Brookhaven¹³.

The spectrometer was 180 gm/cm² thick (0.75 proton mean free paths) and so particles of range \approx 180 gm/cm² were stopped by ionization loss. This energy was 620 MeV/amu for Be, 1100 MeV/amu for O and 1600 MeV/amu for Si. At higher energies where the energy deposit was dominated by the particle interactions, the pions produced, and the subsequent electromagnetic cascades, the fluctuations were very large and depended strongly on where the particle interacted. The spectrometer was thus too thin to make spectral measurements. However, the spectrometer did help differentiate between particles of low charge and high velocity and those of higher charge and lower velocity. In this case the scintillator response turned up (like a relativistic increase) at high energy. This turnup increased as Z increased and is related to the non-linearity of response of the scintillator and to the high energy delta rays which can leave the core of saturation and can penetrate down to the scintillator from the matter in the detectors

above. The net result is to make the separation of adjacent charges more difficult above $\beta \approx 0.8$. The spectrometer, even though not accurate enough to produce energy spectra, helps to resolve this problem.

After mapping, the five pulse height measurements are analyzed to find the charge and energy of each particle. Each event accepted was plotted as a point in a five dimensional space. Concentrations of points occurred where the average pulse heights for the various elements occurred. As the average pulse heights for each element vary with energy, the concentrations of points lie about lines in the 5-dimensional space.

This analysis represents an extension of the technique described previously^{2,14,15,16} for discrete responses. A mathematically rigorous treatment of the technique has been given¹⁷.

In order to find the response lines, we made two dimensional histograms or scatter plots as shown in Figures 2 and 3. The two scintillator pulse heights were, on the average, equal and the Cerenkov pulse heights had small enough variations that we treated their averages as equal. Thus, we had only to determine the concentration lines in three dimensions. The $(S_1 + S_2)/2$ vs. $(C_1 + C_2)/2$ plot in Figure 2 and the spectrometer energy vs. $(C_1 + C_2)/2$ plot in Figure 3 were sufficient for our needs. The lines and the standard deviations (as functions of Z and energy) were determined along each axis for all reasonably abundant elements. It was assumed that only photoelectron statistics contributed to the Cerenkov standard deviation; i.e., that knock-on electron fluctuations were of no concern¹⁸. The Cerenkov standard

deviation at the highest energies was obtained from plots such as the plot for oxygen nuclei given in Figure 3. At high energy the width of the vertical tail is solely due to Cerenkov fluctuations. The Cerenkov standard deviation at any other energy was then scaled like the square root of the Cerenkov signal. The large uncertainty in energy at high energies can be seen in Figure 3.

A computer program was written which finds the distance of the point for each event from the nearest line in terms of standard deviations¹⁷. Each charge line was defined by twelve 5-dimensional points and by linear interpolations between them. Interpolations were also made between charge lines to produce non-integral charge lines. (Charge was allowed to vary continuously and a response surface was defined as a function of Z and energy. The program found the closest point on the surface to the data point). A two dimensional histogram of distance from the nearest line vs. the nearest line is shown in Figure 4. The points in the plot on the right show the projection of this data on the vertical axis. Most of the data occurs between one and two standard deviations from the nearest line. Data close to a line occurs predominantly near integral lines as should be expected. Background events produce a slowly varying continuum, much of it in the tail of the curve.

Figure 4 can be used to find the flux of individual nuclei on the experiment and the background. The projection of abscissa channels 93 and 94 (in the valley between oxygen and neon) onto the ordinate axis is normalized upwards and is plotted as the heavy line in the plot

on the right. The normalization was chosen to make the areas under the tails of the curves equal. The similarity in shape of the tails produced by all data and by channels 93 and 94 is excellent. In fact the tail has roughly the same shape at all charges.

The peak should have the shape of a Maxwell-Boltzmann curve¹⁷. The light line in the plot at the right of Figure 4 is the sum of the heavy background line and a Maxwell-Boltzmann curve. The agreement with the data is seen to be good.

In order to find the number of events for a given particle we integrate under the peak region of this two dimensional histogram. We then make corrections for the background events that lie within the region of integration and for the good events that lie outside the region of integration. The integrals over the ordinate in Figure 4 for total signal and the background are shown in Figure 5. The region of integration is from 0 to 2.3σ .

We find the background under the peak at each charge by multiplying the tail at each charge by the peak background to tail background ratio. The region determined to be more than 99% background events lies above 3.8σ and our plots terminated at 9.2σ . The region which contained about 85% of the signal extends to 2.3σ . The heavy line in Figure 4 is certainly an upper limit to the background under the peak as some oxygen and neon spill into the valley and no allowance is made for the presence of flourine. Since a lower limit is practically zero, we choose the background from 0 to 2.3σ to be half of the heavy line and we allow the systematic error in this background to be equal to this background. The ratio of the background from 0σ to 2.3σ (peak

region) to the background from 3.8σ to 9.2σ (tail region) is found to be 0.286. Thus, multiplying the tail area for each charge (abscissa bin) by 0.286 we obtain the background in the peak region given by the heavy line histogram in Figure 5. The shading denotes the systematic error. The difference between the total histogram and the background histogram is due to single particle events. The fraction of events in the tail of a Maxwell-Boltzmann curve beyond 2.3σ is 15% and is now added in.

We sum counts in appropriate abscissa bins for each element and obtain total counts and statistical and systematic errors. Next, a correction must be applied to account for the inefficiency of the spark chamber and for events lost because of scattered particles that produced a second track in the spark chamber.

The spark chamber efficiency was determined by finding the numbers of events that caused exactly 8 decks, 7 decks, and 6 decks of the 8 deck spark chamber to fire. Assuming the average probability of a deck not firing is Q , the probability of having an event fire N decks is

$$P(N) = \frac{8!}{(8-N)! N!} Q^{8-N} (1-Q)^N$$

Curves of this function are shown in Figure 6. The ratios $P(8)/P(7)$ and $P(7)/P(6)$ indicate that the relative numbers of events that caused 6, 7 and 8 decks to discharge in the particle track obey this probability formula reasonably well. The probability, Q , was determined for each element and for subgroups of events lying at various distances from the nearest charge line described above. The efficiency of the spark chamber is

different for the x and y-views, reflecting known readout inefficiencies in the y view. A plot of the efficiencies is given in Figure 7.

This correction is less than 10% for elements B and above in this flight. However, in our previous flight the chamber had only four decks, and with so little redundant information on the tracks Q could not be determined, and the separation of the primary track from its delta rays was more unreliable. While every attempt was made to take account of these factors in our previous analysis, a Q of 0.02 for a four deck chamber could have resulted in a 20% error in flux since we required a spark to be present on all four decks in both x and y. Further, this effect could have been Z dependant. Unfortunately, there is no way of determining the size or presence of this effect in our earlier data, so these fluxes have to stand as published² with the additional caveat that the fluxes of the elements $3 \leq Z \leq 10$ may be systematically low due to small inefficiencies in the spark chamber.

BACKGROUND

Spark Chamber

It is well known by cosmic ray experimenters that the background intensity falls off rapidly as Z increases away from the very abundant protons and alphas. This is reflected in our data also. In Figure 8, the probability of a second track being registered in the spark chambers is shown to decrease as the charge increases. This probability goes from a few percent at Li to below 1% at C and leads us to believe that trajectory confusion due to backscattering events is not a significant source of error. This is further verified by Table 1 where it is seen

that well identified nuclei are correlated with good spark chamber tracks. The background of well identified events with no spark chamber tracks is probably due to air showers, and falls off rapidly with increasing pulse height. This background makes the identification of Li very difficult.

From this table we see that any procedure which places a requirement that a good track be present greatly enhances the signal to noise ratio and does not significantly bias against good events.

The atmosphere and the material in the experimental apparatus cause cosmic rays to spallate and lose energy. Interactions that caused two or more spatially resolvable particles to pass through the spark chamber were looked for in the data. If two or more tracks diverged from a point in the x-view and the vertical height of this point from the center of the spark chamber equalled the vertical height of a similar point in the y-view, an interaction was considered to have occurred. One such event is shown in Figure 9. We plot the interaction vertices of all such events in both the x and y-views and obtain the scatter plot in Figure 10. The locations of the detectors are indicated and the interactions can be seen to originate in materially dense regions. The number of these events that caused at least 7 or 8 decks to discharge in each of two tracks is 633 or 4% of the single ion events. When the criterion of a good fit was applied to these events they became a negligible fraction. The probability of the spark chamber registering such an event is approximately the square of the probability given in Figure 7 or about 0.8 above B. In the analysis of the data these interaction

events were not explicitly considered. Most of them interacted in the charge module and were accounted for by (1) the background under the Maxwell-Boltzmann curve and (2) the final interaction cross section correction. Perhaps as many as 100 events possessed backscattered interactions from the top of the spectrometer. This is less than 1% of the total events and seems to be an unlikely source for any large systematic error.

The correction for the efficiency of the spark chamber to have more than one track in a view was made assuming the additional tracks were delta rays and hence these events should be included. If some of the multiple track events were actually spallation events, the correction should not be as large as given in Figure 7. The probability of spallation increases with charge. Figure 7 shows the correction to be 0.5% for high charges and so we have overestimated our fluxes at most by this amount.

Maxwellian Distribution

In order to more fully understand the background in the tail of the curve in Figure 4, we looked at the pulse heights of all detectors for 68 carbon events satisfying (1) $33 \leq S_1 \leq 43$ and (2) distance from nearest charge line ≥ 5 . We made 5 categories of events and found the following distribution:

1. 46 (68%) events characterized by
 - a. one detector having an anomalously low or high signal and
 - b. the following detectors having anomalously low signals.

These events are probably interactions.

2. 5(7%) in which the C_2 pulse height was anomalously high, and all other pulse heights were normal. These could be due to a delta ray going through a PMT tube face. (This effect is unimportant in C_1 .)
3. 8(12%) in which one scintillator is too high. These fluctuations are at least 5σ and are unlikely to be caused by Landau fluctuations. They could be due to nuclear excitations of detector atoms.
4. 5(7%) spectrometer signal anomalously large due to the non-Gaussian distribution of signals in the thin (0.75 mean free path) spectrometer.
5. 4(6%) showers and other explanations.

Thus a detailed look at events in the tail of the goodness of fit curve shows that most involve interactions.

In order to account for the possibility that events in categories 2-4 are legitimate, we have included a correction for good events under the background curve from 2.3σ to 9.2σ . We have linearly added 50% of these added events to the systematic error. This correction accounts for a varying amount of the flux. For example the correction is 5% for carbon and 25% for a rare element like Na. This represents the least satisfying part of our data analysis.

Category 2 could have been eliminated if we had divided the Cerenkov phototubes for each detector into two sets and checked for consistency between them.

A correction could have been made for Category 3 by knowing the excitation cross sections, but this category of error is probably common to all composition measurements made with plastic scintillators.

Category 4 could have been eliminated by the use of a thicker spectrometer.

Corrections

Corrections for spallation in the atmosphere are made for the average 3.91 g/cm^2 average depth during the data taking period and for the 7.25 g/cm^2 of experiment thickness through the charge determining module. The mean free paths for the various elements were obtained from Webber et al¹⁴. No errors from uncertainties in the mean free paths are included in our analysis.

A bias was inadvertently introduced in one of our spark chamber track selection criteria that primarily affects the lowest elements. Since the errors in these fluxes are already very large, we have simply corrected Li upward by 10%, Be by 6%, B by 4%, C by 1% and with no corrections for heavier elements. We have linearly increased the respective systematic errors by 3%, 2%, 1% and 0% of the respective abundances. We felt it unjustified to redo our analysis because the results would not be appreciably changed.

Results

The geometrical factor of the 50 cm square by 80.5 cm high experiment is 776 cm^2 star. Live time accounted for 55.67% of the 19 hours and 19 minutes of the data taking period yielding a live exposure time of 38713 seconds. The raw data and all the corrections applied are shown in Table 2. The symbols used in Table 2 are defined in Figure 11.

The resulting fluxes of the elements and the statistical and systematic uncertainties are given in Table 3. The results of a complete analysis without including the spectrometer data is also given. These results are plotted in Figure 12. Various ratios are given in Table 4. The systematic errors play a smaller role in the uncertainty of a ratio

than in the flux because the errors in the numerator and denominator both vary in the same way. The systematic error in the ratio is obtained by assuming the background is either underestimated or overestimated in both elements. The error of a ratio in Table 4 is the square root of the sum of the square of the fluctuation due to systematic errors and the square of the statistical error.

It can be seen in Figure 12 that the background in the region of the light nuclei is substantially reduced by including the spectrometer in the analysis. Also note the effect of the spectrometer in lifting the degeneracy in response between high energy particles of a low charge and lower energy particles of the next higher charge. One might expect the systematic errors in the background correction to produce uniformly high or low abundances for a given analysis. That they do not suggest that the background distributions under the peak and/or the contributions of good events in the tail are not known. They are probably coupled to the analysis method, differently for different charges. It further reflects that a careful analysis of systematic errors is essential to making interexperiment comparisons of absolute intensities.

COMPARISON WITH PREVIOUS DATA

In Table 4 our flux ratios are presented and compared with previously published values.^{15,4} The relative abundances are in generally good agreement, but there are still some differences that are outside the quoted systematic errors, even if we assume other experiments have systematic errors as large as ours.

Previous carbon and oxygen intensity measurements and our data point are shown in Figure 13. There is agreement with Cal Tech¹⁹ and disagree-

ment with the Universities of New Hampshire¹² and Chicago⁴. In order to try to understand the disagreement, we analyzed the first $\sim 10,000$ events in our data with only one selection criterion: that $(S_1 - S_2)/(S_1 + S_2) \leq 0.3$. This criterion is very roughly the criterion used in the experiments of the New Hampshire and Chicago groups which are similar to ours. Neither of these experiments contains a spark chamber, and so if no track could be found, the particle was assumed to be vertically incident. The resulting histogram vs. distance from the nearest charge line is given in Figure 14. A background curve obtained from the flourine valley and a curve of this background plus a Maxwell-Boltzmann distribution are also shown. We find that $\sim 1/3$ of the events that satisfy $2(S_1 - S_2)/(S_1 + S_2)$ are background events according to our analysis.

This may be in part responsible for the differences between intensities. The analysis conducted by the Cal Tech group gives an intensity that agrees with ours. Their telescope is made of solid state detectors and the systematic effects should be the least. Their spectrum, however, is flatter than that of the New Hampshire group at low energy.

In summary, we believe that the discrepancy between the fluxes of Balasubrahmanyam and Ormes² and those of Webber et al.¹², Jullison⁴ and Smith et al.²⁰ is partially due to spark chamber inefficiencies in the former experiment and partially to background rejection criteria in the latter experiments. It is important to resolve this discrepancy, because it affects the interpretation of the C+O/Fe ratio which is dependent upon energy. We have found nothing in this analysis which would lead us to doubt our earlier result that the Fe spectrum is significantly flatter than the C+O spectrum. What is at issue is the relative intensities. If the C+O/Fe ratio at earth can be shown to go below the calculated source ratio at energies above 10 GeV/amu,

then there is no extreme energy dependent propagation model which can explain it, and one must turn to energy dependent models at the source or different sources of different species of cosmic rays.

We hope to resolve this discrepancy by flying a spectrometer sufficiently deep to measure energy along with a gas Cerenkov detector to calibrate the spectrometer for $Z > 1$ nuclei at 15 GeV/amu. The data will then be analyzed using the techniques described here.

REFERENCES

1. High Energy Primary Cosmic Ray Program of Goddard Space Flight Center, J. F. Ormes, V. K. Balasubrahmanyam, Proc. 11th International Conf. on Cosmic Rays, Acta Physica Hungaricae, 29, Suppl. 4, 397, (1970).
2. Results on the Energy Dependence of the Cosmic Ray Charge Composition V. K. Balasubrahmanyam and J. F. Ormes, Astrophysical Journal, 186, 109, (1974) and references therein.
3. Charge Dependence of the Energy Spectra of Cosmic Rays, J. F. Ormes V. K. Balasubrahmanyam, Nature, 241, 95, 1973.
4. Cosmic Ray Nuclear Composition above 20 GeV/nucleon, E. Juliusson, 13th International Cosmic Ray Conf., 1, 178, (1973) and Astrophysical Journal, 191, 331, 1974.
5. Cosmic Ray Sources: Evidence for Two Acceleration Mechanisms, R. Ramaty, V. K. Balasubrahmanyam and J. F. Ormes, Science, 180, 731, 1973.
6. Interpretation of the Chemical Composition of High Energy Cosmic Rays, C. J. Cesarsky and J. Adouze, 13th International Cosmic Ray Conf. 1, 189, (1973).
7. The Energy Spectra of the Cosmic Ray Nucleonic and Electronic Components, W. R. Webber, Conference Papers, 13th International Cosmic Ray Conf., 5, 3568, (1973).
8. Measurement of the Primary Cosmic Electron Spectrum from 10 GeV to about 250 GeV, R. F. Silverberg, Ph.D., Thesis, University of Maryland (1973), to be published.

9. Spark Chamber Track Finding Program, J. F. Arens, submitted to IEEE Transactions on Nuclear Science (1974).
10. Development of Spark Chambers for Use in Measurements of the Charge Spectrum of High Energy Cosmic Rays, J. F. Arens, G. F. Cooper, C. R. Greer, J. Jellison, A. B. MacNee, J. F. Ormes, M. J. Ryan IEEE Transactions on Nuclear Science, NS20, 1 (1973).
11. Energy Spectra of Individual Cosmic Ray Elements with $12 \leq Z \leq 28$, M. H. Israel, J. Klarman, R. C. Maehl, W. R. Binns, 13th International Cosmic Ray Conf. 1, 255 (1973).
12. Differences in the Spectra of Cosmic Ray Nuclear Species Below ~ 5 GeV/Nuc, W. R. Webber, J. A. Lezniak, J. Kish, 13th International Cosmic Ray Conf., 1, 248, (1973).
13. Energy Calibration of a Cosmic Ray Ionization Spectrometer, H. Whiteside, C. J. Crannell, H. Crannell, J. F. Ormes, M. J. Ryan, W. V. Jones, Nucl. Inst. and Meth., 109, 375, (1973).
14. A Technique for Utilizing Multiple Measurements to Assign Charges and Remove Background in a Cosmic Ray Experiment, T. Raymond, J. F. Ormes and V. K. Balasubrahmanyam, Bull. Am. Phys. Soc., 16, 1971.
15. Studies of the Chemical Composition of Cosmic Rays with $Z = 3-30$ at High and Low Energies, W. R. Webber, S. V. Damle, J. Kish, Astrophysics and Space Science, 15, 245, (1972).
16. Charge Composition of High Energy Primary Cosmic Ray Nuclei, R. D. Price, Ph.D. Thesis, X-661-74-71, excerpts to be published.

17. Multielement Detector Data Analysis, J. F. Arens, A. J. Fisher, J. F. Ormes, to be published in Nuclear Instruments and Methods, 1974.
18. On the Suitability of Cerenkov Counters for Analysing the Charge Composition of the Primary Cosmic Radiation, B. Dayton, N. Lund and T. Risbo, Danish Space Research Institute Report, July 1969.
19. The Elemental Abundance Ratios of Interstellar Secondary and Primary Cosmic Rays, J. W. Brown, E. C. Stone, R. E. Vogt, 13th International Cosmic Ray Conf., 1, 556, (1973).
20. A Measurement of Cosmic Ray Rigidity Spectra above 5 GV/C of Elements from Hydrogen to Iron, L. H. Smith, A. Buffington, G. F. Smoot, L. W. Alvarez, W. A. Wahlig, Ap. J., 180, 987, (1973).

FIGURE CAPTIONS

- Figure 1 Experiment configuration.
- Figure 2 Scatter plot of average scintillator pulse height vs. average Cerenkov pulse height. Solid lines are drawn by eye.
- Figure 3 Scatter plot of summed spectrometer pulse heights vs. average Cerenkov pulse height for oxygen. Solid line is drawn by eye.
- Figure 4 Scatter plot of distance from nearest charge line vs. nearest charge. Plot at right is projection of data on vertical axis. Heavy line is background. Light line is background plus a Maxwell-Boltzmann curve normalized to peak data point.
- Figure 5 Signal and background. The heavy line is background; the shading shows the range of the systematic error. The signal as shown by the light line is coincident with the background between low elements but is higher than background between higher element peaks due to the wider tails.
- Figure 6 Probability of a track containing N decks with discharges in the track in an 8 deck spark chamber vs. the probability of a deck not discharging in the track.
- Figure 7 Probability of a particle track discharging 7 or 8 decks.
- Figure 8 Probability of a particle track that discharged 7 or 8 decks to be accompanied by another 7 or 8 discharged deck track.
- Figure 9 X and Y views of spark chamber that recorded event with two tracks. Each dot represents two wires in the wire grid spark

chamber. "L" denotes the left hand wire discharged; "J" the right hand wire; and "U" both wires.

Figure 10 Coordinates of interaction vertices in X and Y-views. Interactions occur where massive parts of the experiment lie.

Figure 11 Definition of regions under the Maxwellian curve.

Figure 12 Abundances with and without using the spectrometer data in the analysis.

Figure 13 Previously measured carbon and oxygen abundances and our data point.

Figure 14 Number of events vs. distance from nearest charge line for events that satisfy $(S_1 - S_2)/(S_1 + S_2) \leq 0.3$. The expected Maxwellian curve and the background, given by scaling up the flourine valley, are also given.

TABLE 1
EFFICIENCY TABLE

$\frac{S_1+S_2}{2}$	Distance from line in units of σ					
	0-2	2-4	4-8	None		
0-18	337	605	1199	8	0	Number
	213	168	180	57	1	of
	14	14	17	1	≥ 2	tracks
	Distance from line					
18-36	78	156	1074	8	0	Number
	271	178	288	0	1	of
	2	10	22	0	≥ 2	tracks
	Distance from line					
36-54	32	50	581	5	0	Number
	431	278	271	0	1	of
	3	1	20	0	≥ 2	tracks
	Distance from line					
54-72	22	28	344	9	0	Number
	293	173	156	13	1	of
	2	1	13	0	≥ 2	tracks
	Distance from line					
72-190	6	16	504	34	0	Number
	243	168	282	35	1	of
	2	0	15	1	≥ 2	tracks

The total data consists of 168527 events. The first 10000 events were analysed and 714 tracks were found that passed outside C_1 . 8922 of the remaining events have $(S_1+S_2) / 2 < 190$ and are included in this table. Each track must discharge 7 or 8 decks. The column labeled "none" contains events that lie closest to the helium or iron lines or that have multiple minima. Multiple minima can occur if an event lies very far from the response surface. Note that no selection on the consistency of S_1 and S_2 has been made.

TABLE 2

	bins	$N_{0-2.29\sigma}$	N_a	P_{sig}	P_{stat}	P_{sys}	Q_{sig}	Q_{stat}	Q_{sys}	ϵ_1	ϵ_2	i.c.	g.f.	Flux	ΔF_{stat}	ΔF_{sys}
Li	24-33	1016	374	1224	38	192	1346	42	232	.74	.948	.798	3004	.798	.025	.138
Be	37-43	574	236	693	28	121	735	30	135	.86	.968	.775	3004	.379	.015	.070
B	47-54	1526	528	1836	46	272	1909	48	291	.91	.981	.755	3004	.943	.023	.144
C	55-65	5018	775	5977	84	400	6037	85	400	.925	.991	.687	3004	3.191	.045	.211
N	66-74	1438	710	1744	45	366	1744	45	366	.93	.995	.686	3004	.915	.024	.192
O	75-89	4401	693	5243	78	358	5243	78	358	.935	.995	.663	3004	2.831	.042	.193
F																
Ne	94-106	742	259	893	32	134	893	32	134	.94	.995	.653	3004	.487	.017	.073
Ne	107-113	202	110	245	17	56	245	17	56	.94	.995	.664	3004	.131	.009	.030
Mg	114-127	785	134	936	33	69	936	33	69	.94	.995	.621	3004	.537	.019	.040
A	128-132	117	66	142	13	34	142	13	34	.94	.995	.631	3004	.080	.007	.019
Si	133-147	674	98	802	31	51	802	31	51	.94	.995	.590	3004	.484	.019	.031

bins denotes bins along abscissa in Figure 5

$N_{0-2.29\sigma}$, N_a , N_b , N_c are defined in Figure 11

$$\eta = N_b/N_a = 0.273$$

$$f = N_c/N_a = 0.55$$

$$G = \text{Number of good events in tail} = 0.25 N_a (1+f) = 0.3875 N_a$$

$$g_x = \text{Area under Maxwellian curve/Area under Maxwellian curve from 0 to } 2.29 \sigma = 1.181$$

$$P_{sig} = \text{Number of good events} = (N_{0-2.29\sigma} - \eta N_a) g_x + G = 1.181 N_{0-2.29\sigma} + 0.065 N_a$$

$$P_{stat} = \text{Statistical error} = \sqrt{1.181^2 N_{0-2.29\sigma} + 0.065^2 N_a} = \sqrt{1.395 N_{0-2.29\sigma} + 0.0042 N_a}$$

$$P_{ys} = \text{Systematic error} = \eta g_x N_a + 0.5 G = 0.516 N_a$$

$$Q_{sig} \text{ has correction for analysis error. } Q_{sig} = P_{sig} \times (1.10 \text{ for Li, } 1.06 \text{ for Be, } 1.04 \text{ for B, } 1.01 \text{ for C, } 1.00 \text{ for others)}$$

$$Q_{stat} \text{ has correction for analysis error. } Q_{stat} = P_{stat} \times (1.10 \text{ for Li, } 1.06 \text{ for Be, } 1.04 \text{ for B, } 1.01 \text{ for C, } 1.00 \text{ for others)}$$

$$Q_{sys} \text{ has correction for analysis error. } Q_{sys} = P_{sys} + Q_{sig} \times (0.03 \text{ for Li, } 0.02 \text{ for Be, } 0.01 \text{ for B, } 0.0 \text{ for others)}$$

$$\epsilon_1 = \text{Efficiency for one or more tracks in spark chamber}$$

$$\epsilon_2 = 1 \text{ minus efficiency for two or more tracks in spark chamber}$$

$$\text{i.c.} = \text{Interaction correction}$$

$$\text{g.f.} = \text{Geometrical factor}$$

$$\text{Flux} = Q_{sig} / \epsilon_1 \epsilon_2 (\text{i.c.}) (\text{g.f.})$$

$$\Delta F_{stat} = Q_{stat} / \epsilon_1 \epsilon_2 (\text{i.c.}) (\text{g.f.})$$

$$\Delta F_{sys} = Q_{sys} / \epsilon_1 \epsilon_2 (\text{i.c.}) (\text{g.f.})$$

REPRODUCIBILITY OF THE ORIGINAL PAGE IS POOR

TABLE 3

Element	With Spectrometer			Without Spectrometer		
	Flux	Errors		Flux	Errors	
		Statistical	Systematic		Statistical	Systematic
Li	.82	.03	.15	1.18	.03	.10
Be	.39	.02	.07	.50	.02	.10
B	.96	.02	.15	1.00	.02	.21
e	3.22	.05	.23	3.35	.04	.23
N	.94	.02	.21	.84	.02	.20
O	2.86	.04	.21	2.71	.04	.26
F						
Ne	.50	.02	.08	.43	.02	.09
Na	.14	.01	.03			
Mg	.54	.02	.04	.52	.02	.06
Al	.082	.007	.02			
Si	.49	.02	.03	.53	.02	.04

Units are number/m² sec ster

TABLE 4

Ratio of Fluxes	With Spectrometer	Webber et al ¹⁵ > 1GeV/amu	Juliusson ⁴ @6.0gm/cm ² 1 GeV/amu
Be/B	0.40 ± .02	.293 ± .010	0.38
Li/O	0.28 ± .03	.192 ± .004	0.27
Be/O	0.135 ± .02	.101 ± .003	0.15
B/O	0.34 ± .03	.345 ± .005	0.39
C/O	1.13 ± 0.02	1.13 ± .02	1.17
N/O	0.325 ± .05	0.286 ± .005	0.33
Ne/O	0.17 ± .02	0.174 ± .006	0.16
Na/O	0.047 ± .009	0.030 ± .002	0.04
Mg/O	0.190 ± .007	0.204 ± .005	0.20
Al/O	0.028 ± .006	0.030 ± .002	0.04
Si/O	0.171 ± .007	0.137 ± .004	0.15
Li+Be+B/C+N+O	0.31 ± 0.03	0.265 ± .01	0.324

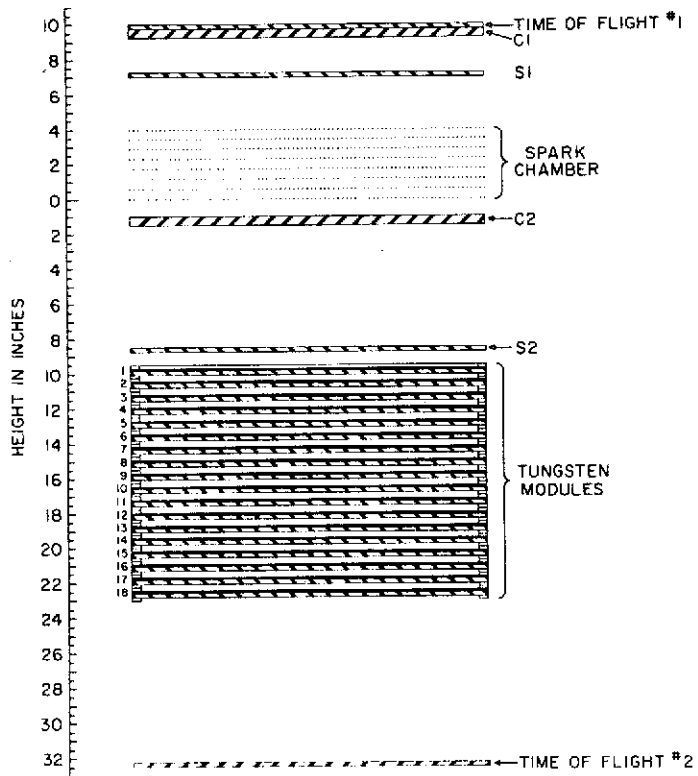
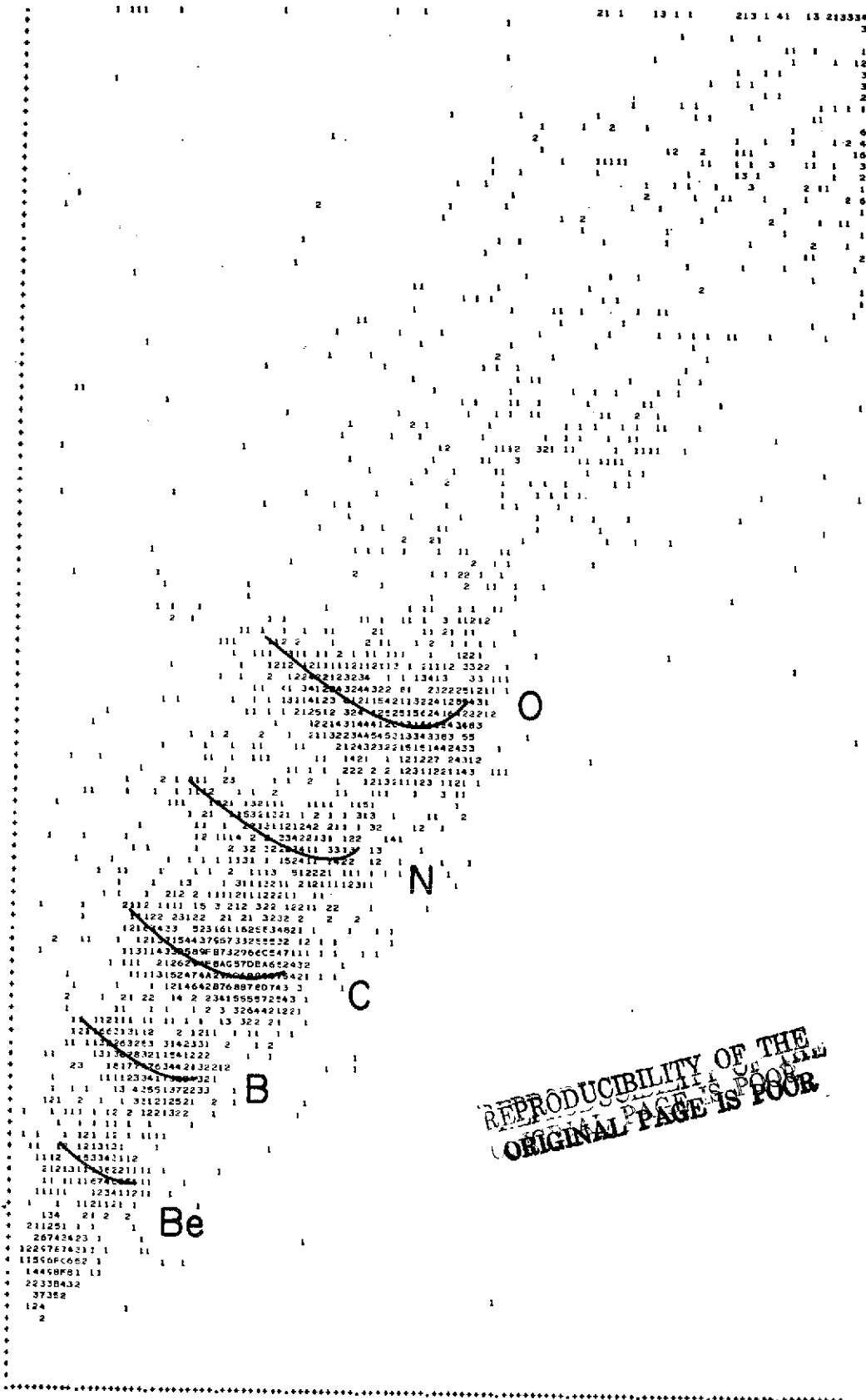


Fig. 1

SCINTILLATOR PULSE HEIGHT



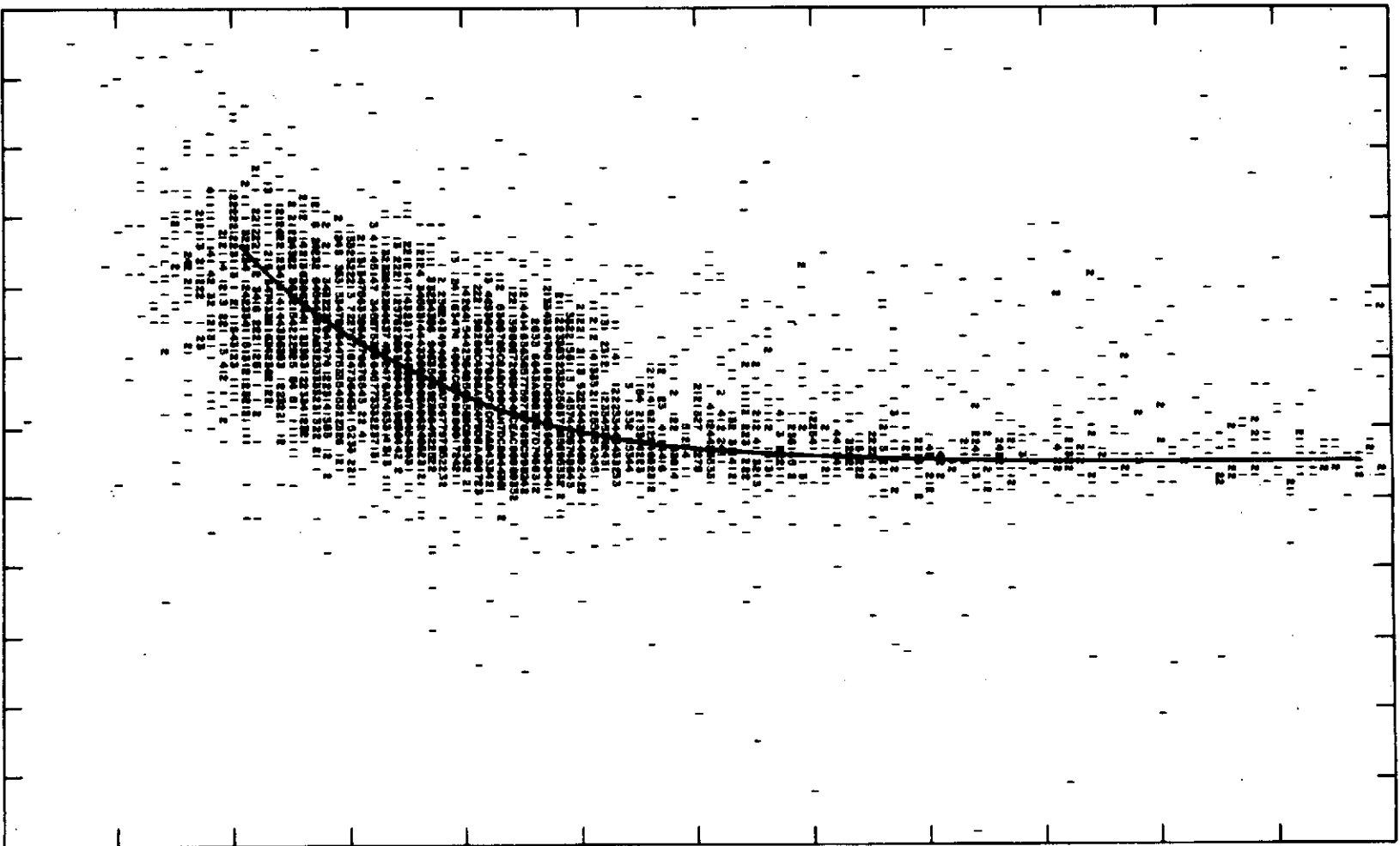
REPRODUCIBILITY OF THE
 ORIGINAL PAGE IS POOR

CERENKOV PULSE HEIGHT

Fig. 2

REPRODUCTION OF THE ORIGINAL PAGE IS POOR

TOTAL SPECTROMETER PULSE HEIGHT



CERENKOV PULSE HEIGHT

Fig. 3

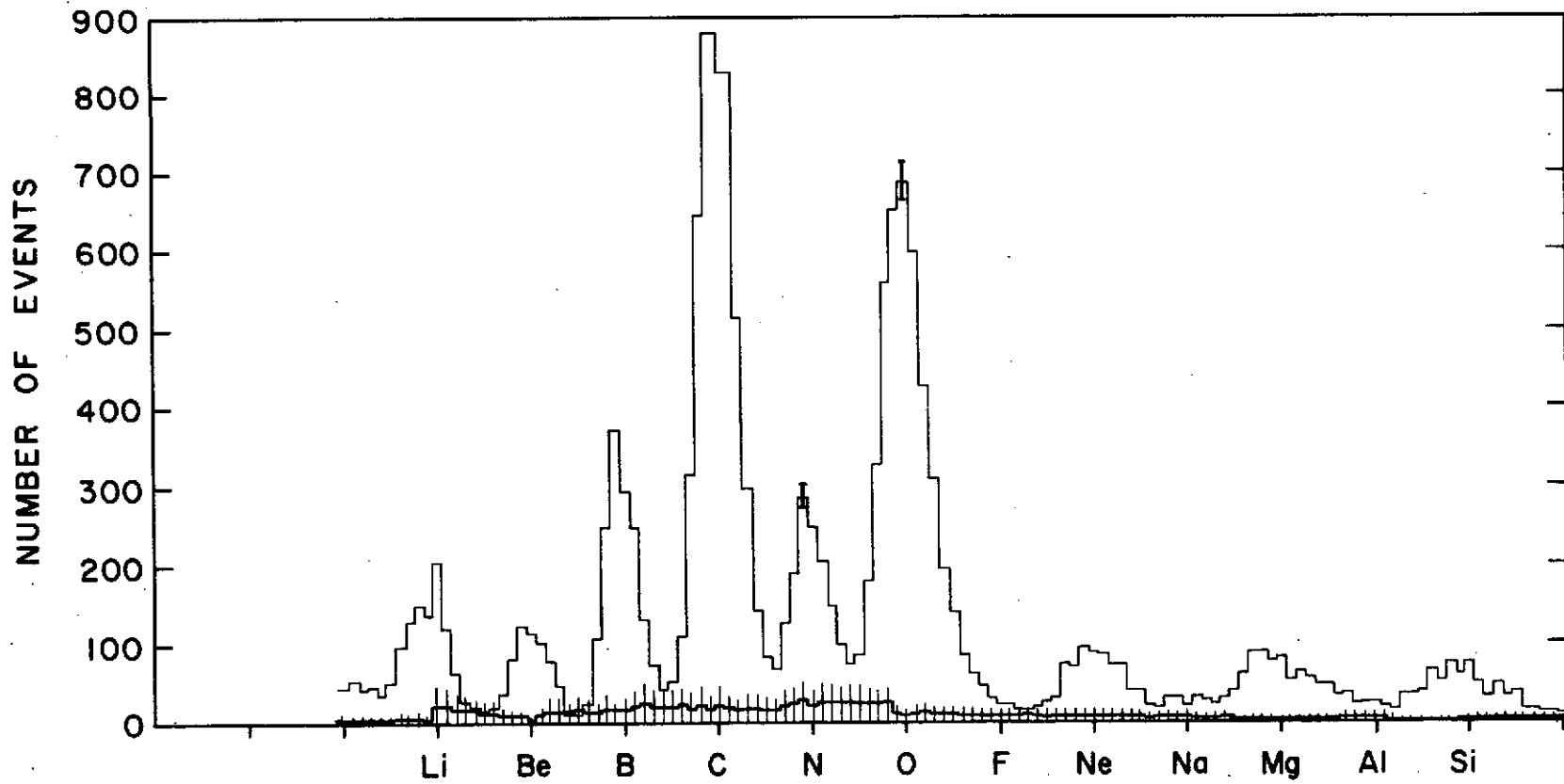


Fig. 5

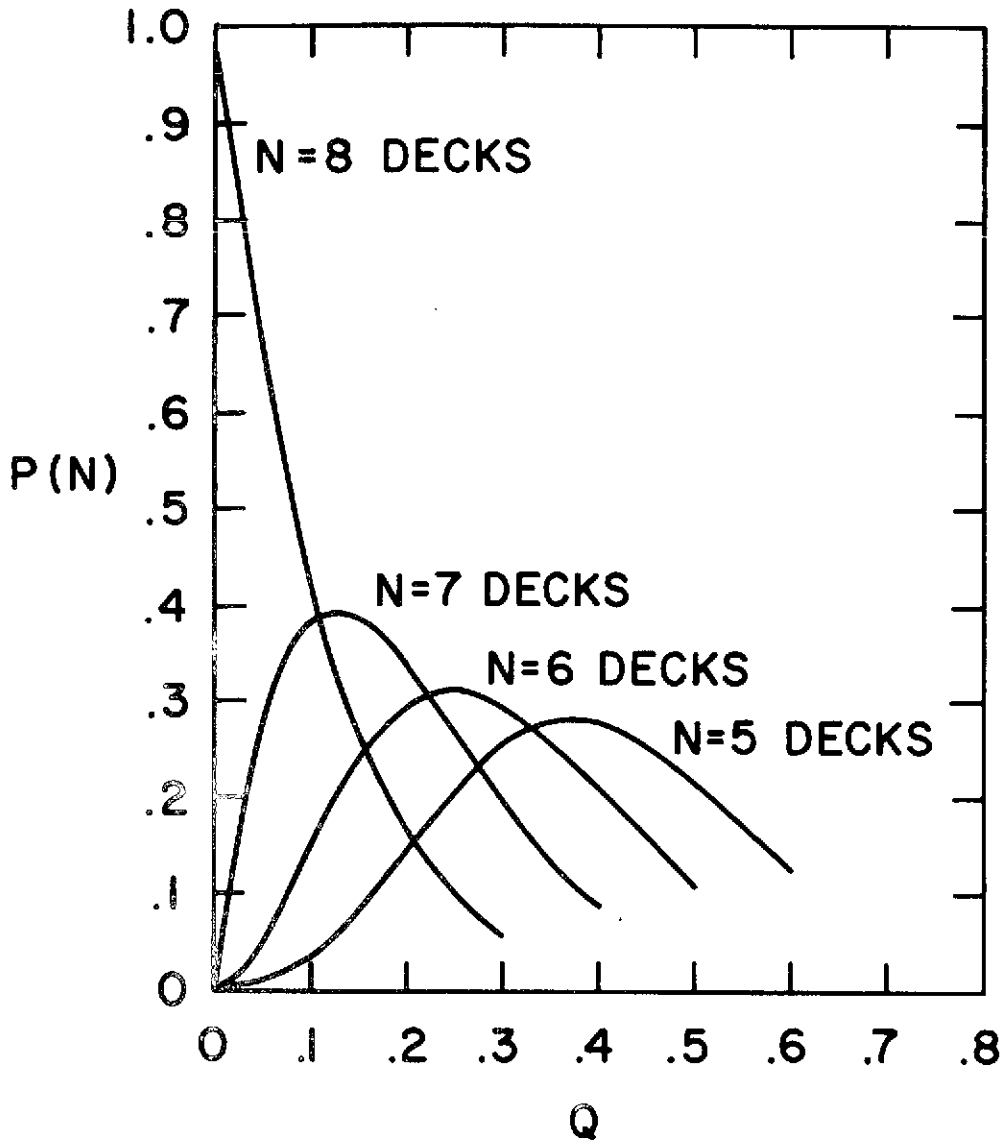


Fig. 6

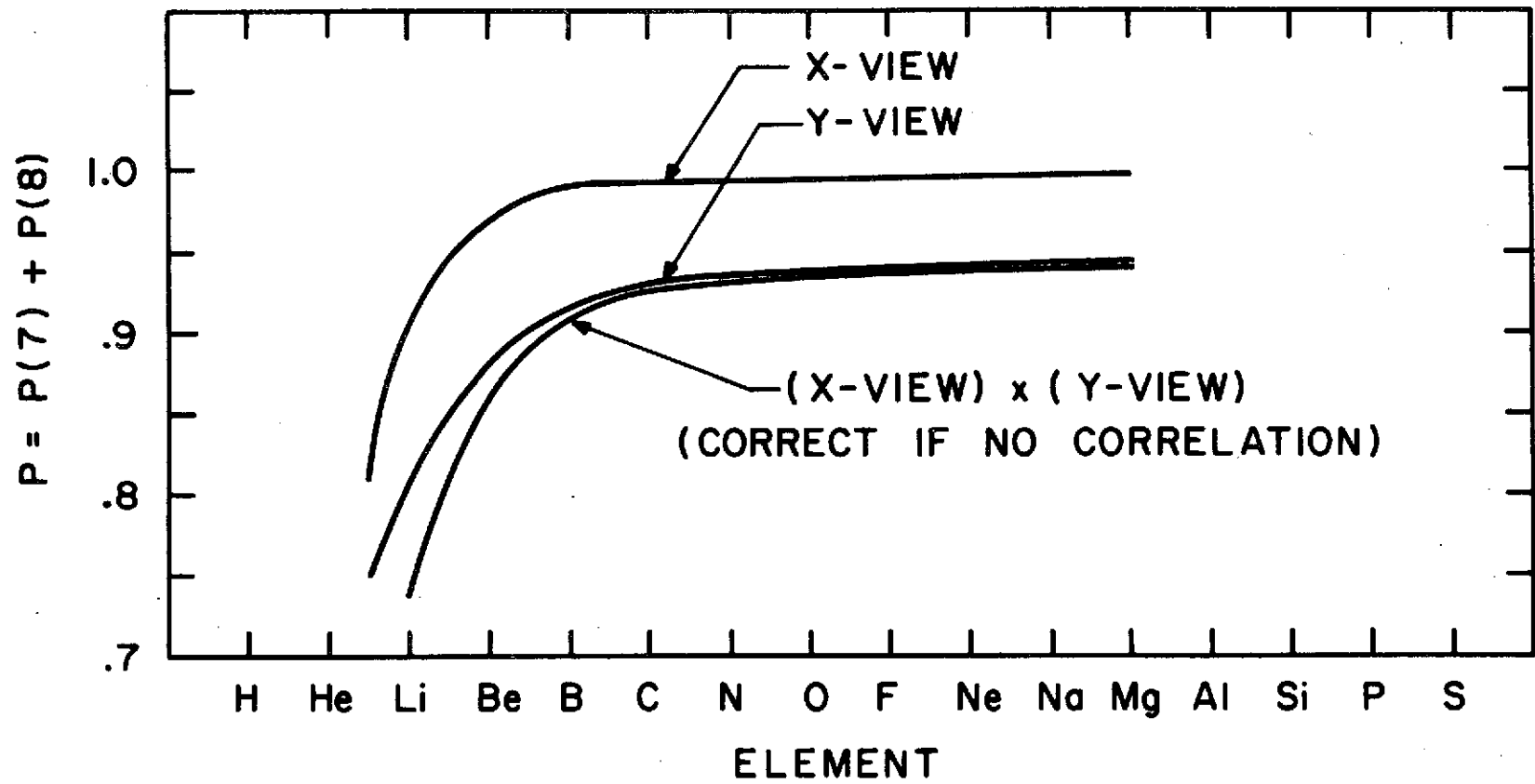


Fig. 7

PROBABILITY OF 2nd TRACK
IN X OR Y-VIEWS

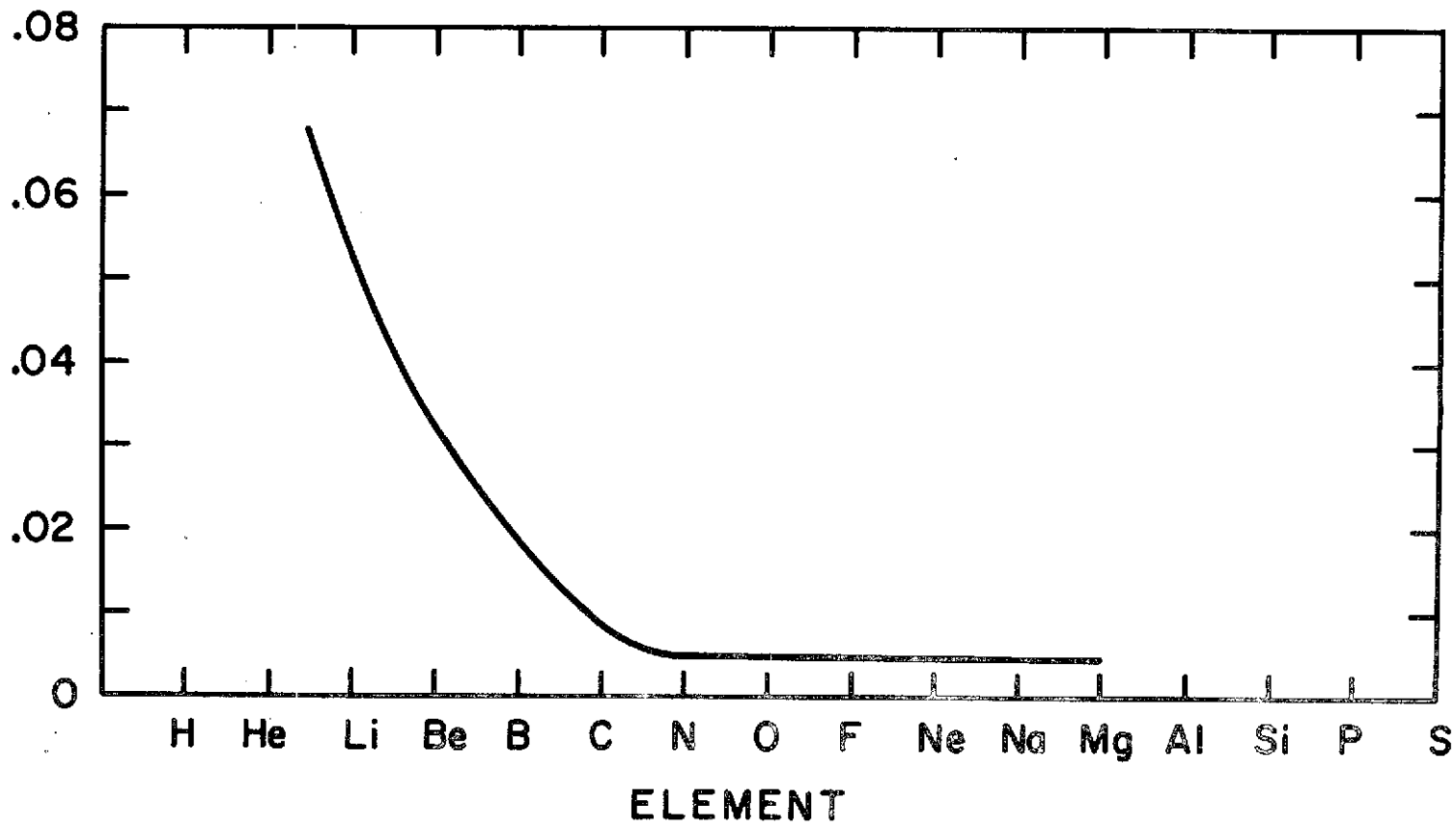


Fig. 8

REPRODUCIBILITY OF THE ORIGINAL PAGE IS POOR

2 1

.....J.....L.....JL.....

.....L.....L.....

.....U.....

.....L.....L.....

.....L.....U.....

.....J.....JL.....

.....J.....L.....JL.....

.....L.....JL.....L.....

2 1

1 2

.....JJ.....J.....L.....

.....L.....J.....

.....JJ.....

.....L.....L.....

.....JJ.L.....L.....

.....L.L.....J.....

.....JL.J.L.....

.....L.L.L.L.L.....L.....

Fig. 9 1 2

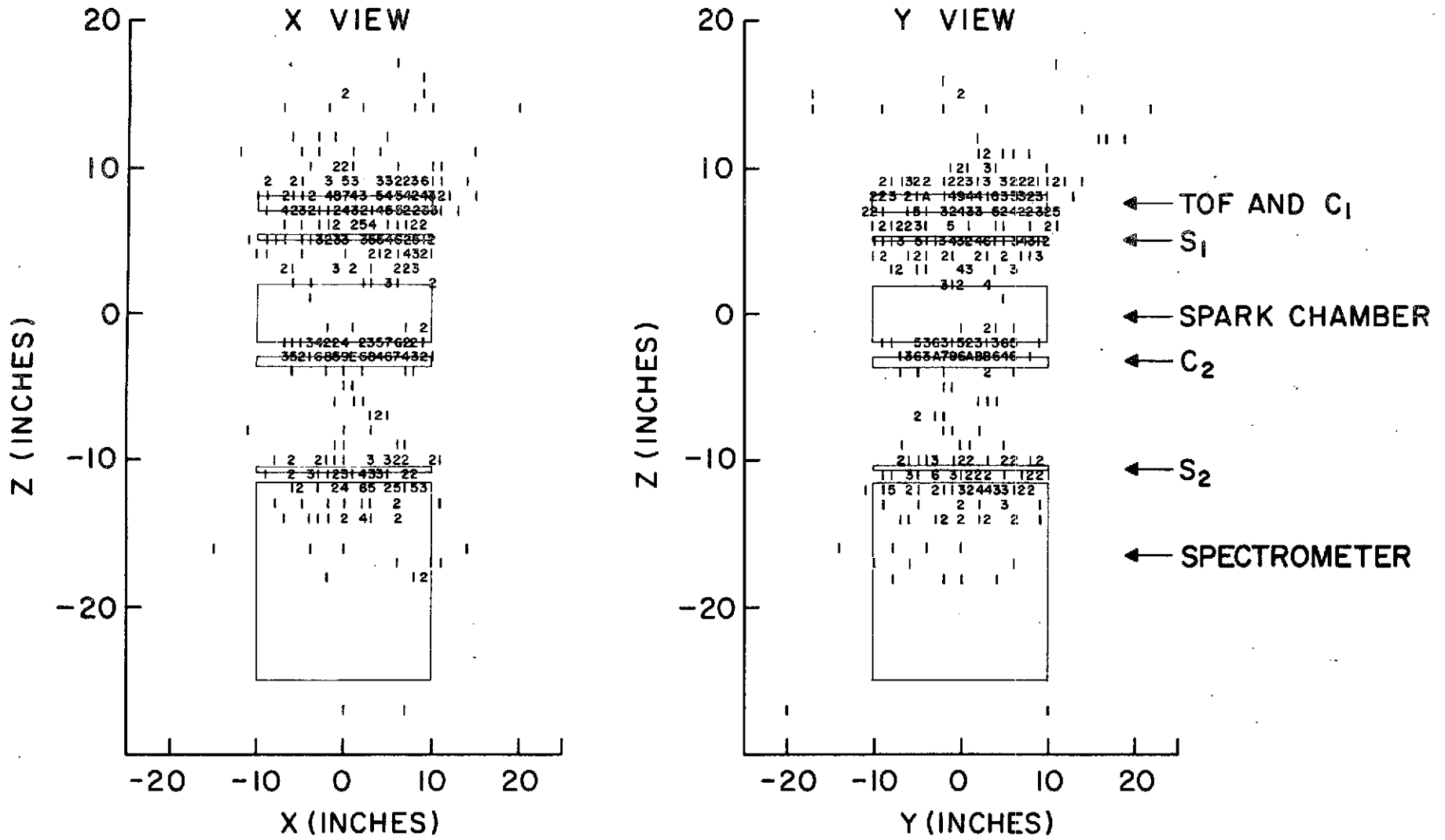


Fig. 10

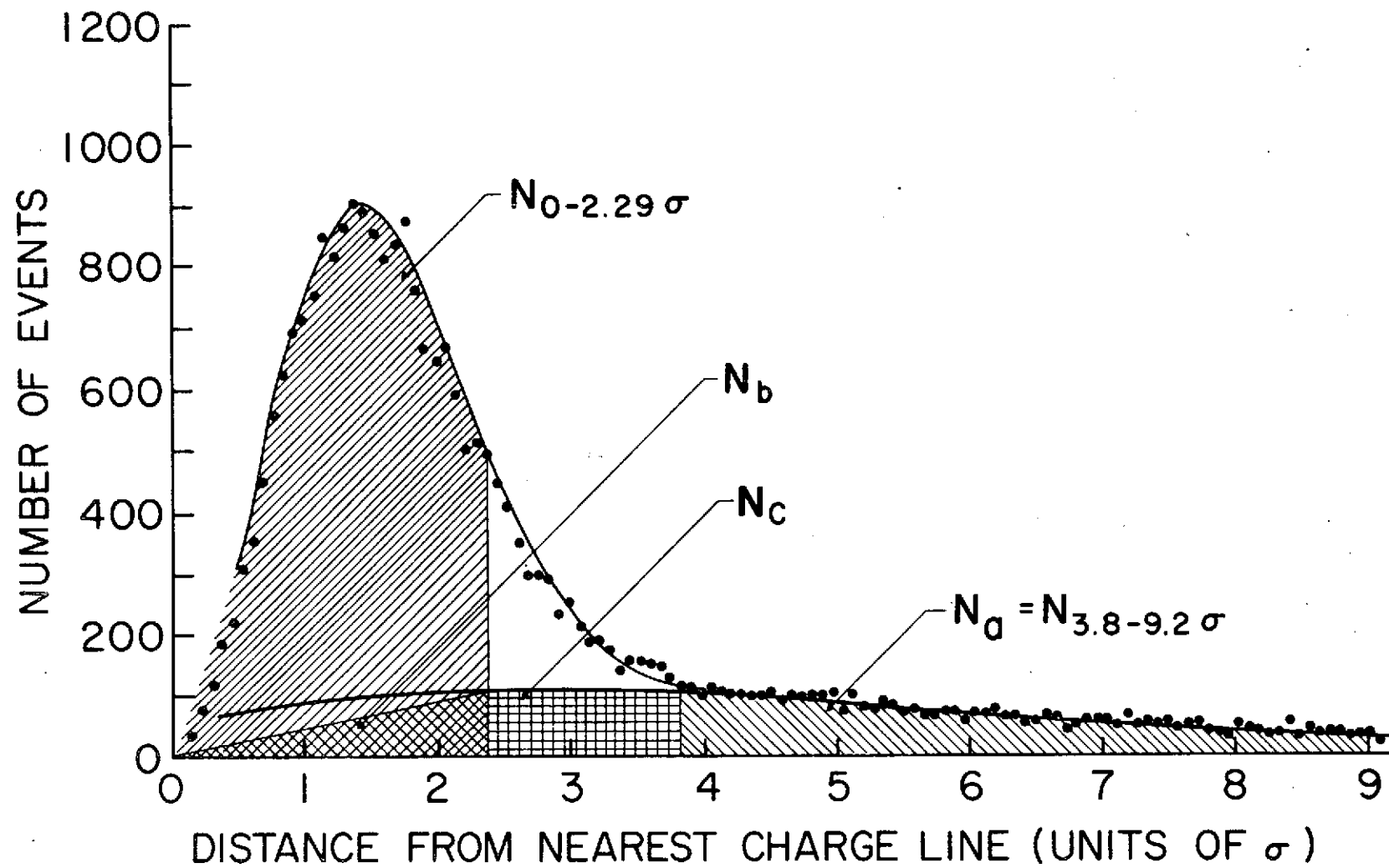


Fig. 11

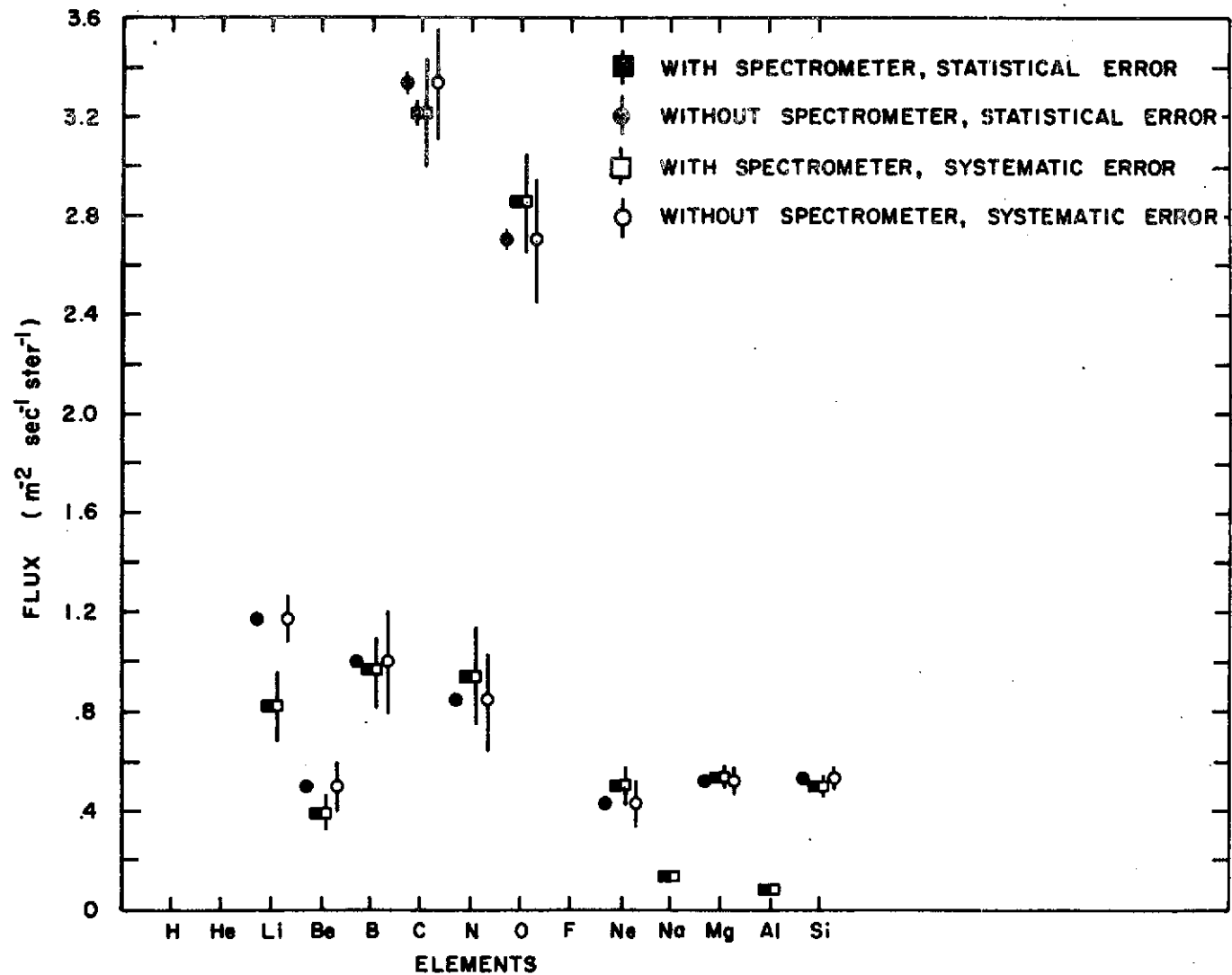


Fig. 12

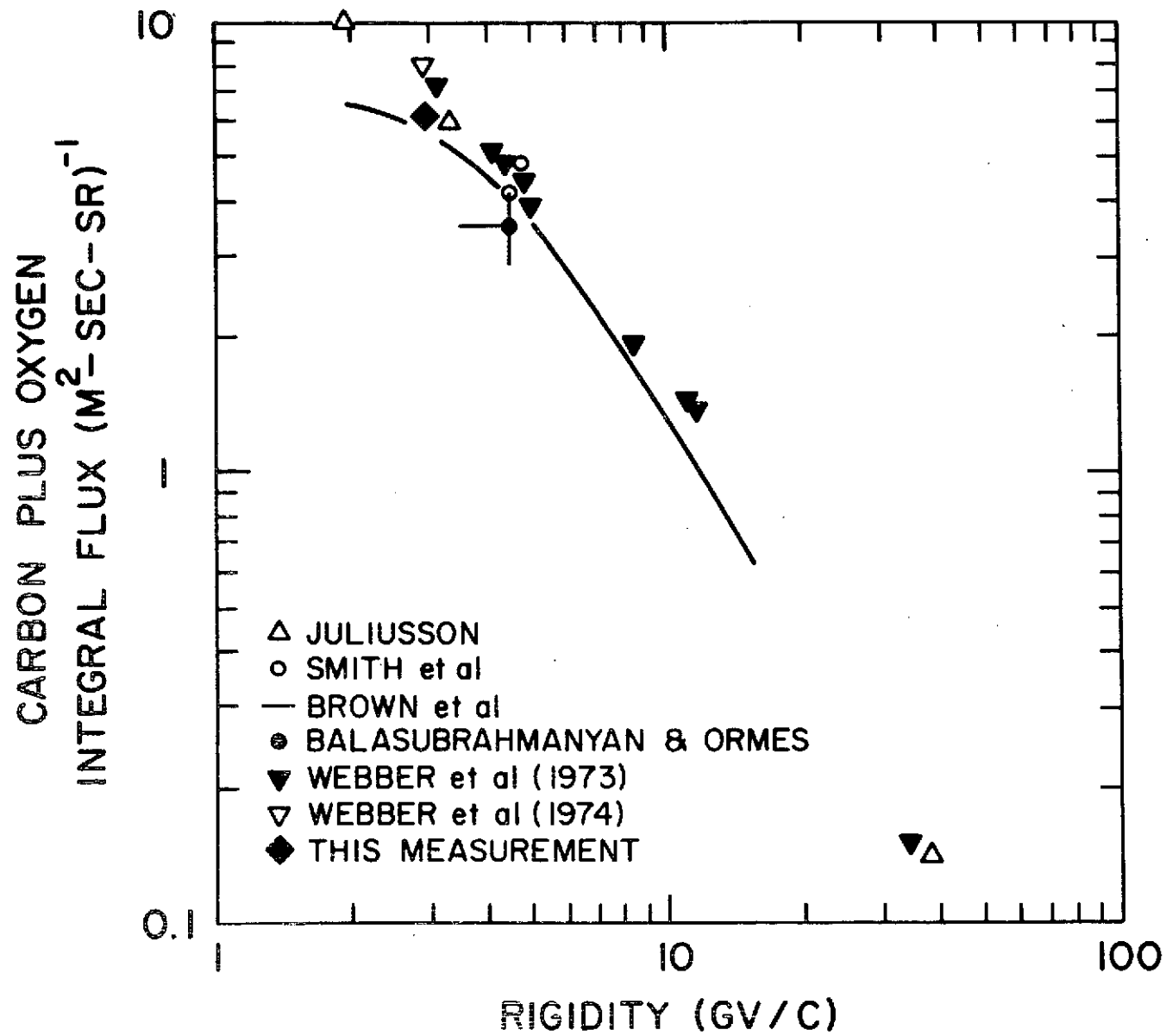


Fig. 13

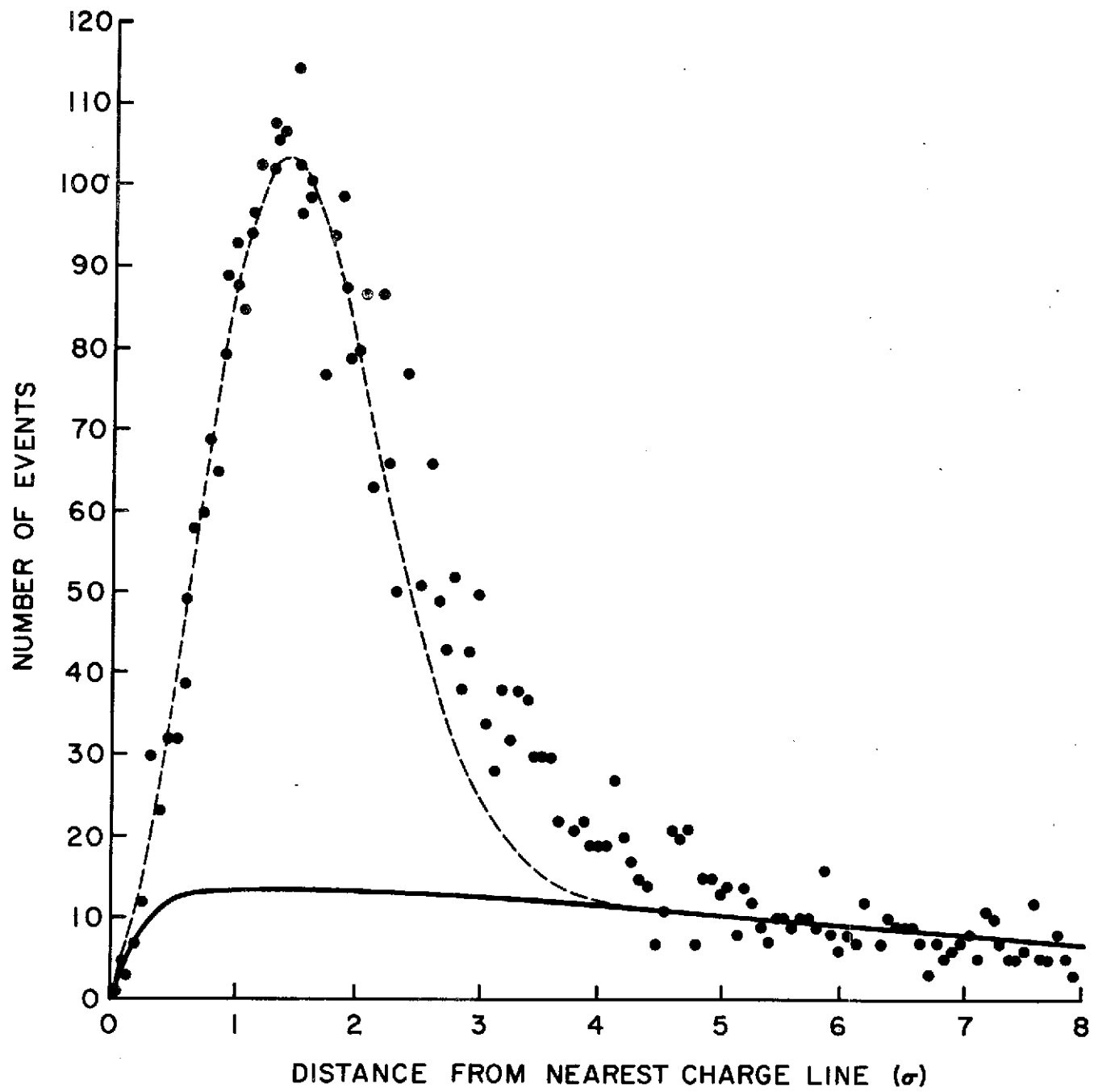


Fig. 14